Mechanisms of Ageing and Development 213 (2023) 111836

Contents lists available at ScienceDirect

Mechanisms of Ageing and Development

journal homepage: www.elsevier.com/locate/mechagedev

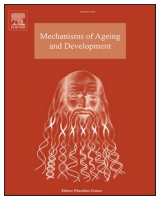

DYRK1B inhibition exerts senolytic effects on endothelial cells and rescues endothelial dysfunctions

Francesca M. Pramotton [a,b,1], Asra Abukar [b,c,1], Chantelle Hudson [d], James Dunbar [d], Andrew Potterton [d], Simone Tonnicchia [a,b], Andrea Taddei [d], Edoardo Mazza [a,b], Costanza Giampietro [a,b,c,*]

[a] Swiss Federal Laboratories for Materials Science and Technology (EMPA), Dübendorf 8600, Switzerland
[b] Department of Mechanical and Process Engineering, ETH Zurich, Zurich 8092, Switzerland
[c] Senecell AG, Zurich 8057, Switzerland
[d] Benevolent AI, W1T 5HD London, UK

ARTICLE INFO

Keywords:
DYRK1B
Endothelial senescence
Adherens junctions
Vascular permeability
Endothelial dysfunction

ABSTRACT

Aging is the major risk factor for chronic disease development. Cellular senescence is a key mechanism that triggers or contributes to age-related phenotypes and pathologies. The endothelium, a single layer of cells lining the inner surface of a blood vessel, is a critical interface between blood and all tissues. Many studies report a link between endothelial cell senescence, inflammation, and diabetic vascular diseases. Here we identify, using combined advanced AI and machine learning, the Dual Specificity Tyrosine Phosphorylation Regulated Kinase 1B (DYRK1B) protein as a possible senolytic target for senescent endothelial cells. We demonstrate that upon induction of senescence in vitro DYRK1B expression is increased in endothelial cells and localized at adherens junctions where it impairs their proper organization and functions. *DYRK1B* knock-down or inhibition restores endothelial barrier properties and collective behavior. DYRK1B is therefore a possible target to counteract diabetes-associated vascular diseases linked to endothelial cell senescence.

1. Introduction

Senescence is a cellular program characterized by phenotypes including irreversible proliferative arrest, resistance to apoptosis, altered transcription profile and metabolism, a senescence-associated secretory phenotype (SASP), and morphological changes such as the increase of cytoplasmic volume, the presence of multiple nuclei, and the flattening of the cells (Beck et al., 2020; Gonzalez-Gualda et al., 2021). Cell senescence contributes to embryonic development and tissue repair as well as inflammation, tissue aging and pathological diseases by release of the SASP, which is both pro inflammatory and pro fibrotic and spreads the senescence phenotype to neighboring cells (Rhinn et al., 2019). In the latter case, removing senescent cells from aging tissues can delay tissue dysfunction (Baker et al., 2011; Xu et al., 2018).

The presence of senescent endothelial cells has been documented in vivo (Fenton et al., 2001) to be associated with cardiovascular diseases, along with diabetes (Lu et al., 2013) where barrier functions are impaired due to increased endothelial permeability (Kimura et al., 1993; Hadi and Suwaidi, 2007).

An option to eliminate detrimental senescent cells is the use of senolytics, a class of compounds that target intracellular pathways activated in senescent cells (Kirkland and Tchkonia, 2020).

Here, we took an integrative approach to leverage cellular senescence relevant data and artificial intelligence in drug target identification to identify new senolytic targets. Using machine-learning models for gene target prioritization in combination with omics- based analysis, we aimed to find putative drug targets to activate apoptotic death in senescent cells in a cell type specific manner. These predictions were triaged with supporting evidence derived from the Benevolent Knowledge Graph (Paliwal et al., 2020; Richardson et al., 2020; Sharma, Tiwari et al., 2020), where we identified the dual specificity tyrosine phosphorylation regulated kinase 1B protein (DYRK1B) as a possible senolytic target that was predicted to be highly relevant for senescent endothelial cells. To identify disease indications for target validation we

* Correspondence to: Empa – Materials Science and Technology, Überlandstrasse 129, CH-8600 Dübendorf, Switzerland.
E-mail address: costanza.giampietro@empa.ch (C. Giampietro).
[1] These authors equally contributed to the work.

https://doi.org/10.1016/j.mad.2023.111836
Received 12 December 2022; Received in revised form 15 May 2023; Accepted 6 June 2023
Available online 8 June 2023

further used our Benevolent Platform™, which mapped senescent endothelial cells to the progression of diabetic nephropathy (DN) and diabetic retinopathy (DR).

DYRK1B is a member of a highly conserved family of protein kinases that control several signaling pathways involved in a wide range of cellular functions such as cell survival, proliferation, differentiation, and senescence (Aranda et al., 2011; Soppa and Becker, 2015; Boni et al., 2020). The abnormal expression or activation of DYRK proteins has been associated with several human pathologies (Boni et al., 2020), including metabolic diseases (Abu Jhaisha et al., 2017). Interestingly, alterations in cell metabolism have been identified in several age-related diseases associated with a dysfunctional vasculature, such as type 2 diabetes (Eelen et al., 2015).

In the present paper, we demonstrated that DYRK1B expression was increased in pathological DN derived endothelial cells and in glucose-induced senescent endothelial cells derived from either the kidney or retina, where it specifically impaired adherens junction organization and functions. Indeed, increased levels of DYRK1B correlated with an impairment in the control of monolayer permeability, as well as in the proper cell orientation in response to flow.

Moreover, we proved that the knock-down of Dyrk1B or its inhibition by small molecule treatment was sufficient to drive senescent cell apoptosis, allowing for the repopulation with healthy cells to preserve the structural integrity of adherens junctions, and partially rescue monolayer barrier functions and collective response to flow.

Finally, in addition to the role of DYRK1B in sustaining the senescence phenotype, we also provided compelling evidence of the molecular basis of how DYRK1B directly caused impaired adherens junction organization in senescent cells. DYRK1B was localized at cell-cell contacts of senescent cells, where it associated with p120-CATENIN and VE-CADHERIN dismantling the adherens junction complexes, thus impairing endothelial functions. DYRK1B is therefore emerging as a possible candidate target to alleviate DN and DR phenotype by removing senescent cells and restoring barrier integrity.

2. Materials and methods

2.1. Cell culture

Primary human umbilical vein endothelial cells (HUVEC; Promocell), primary human retinal microvascular endothelial cell (Cell Systems), primary human renal glomerular endothelial cell (HRGEC, ScienCell), primary human diabetic kidney endothelial cells (Cell Biologics), and primary bovine aortic endothelial cells were grown in Endothelial Cell Growth Medium (C-22010, Promocell) and were maintained at 37 °C and 5% CO_2. In all the experiments endothelial cells were seeded at high initial density (450 cell/mm2, immediately confluent condition) and grown in static conditions for 72 h to generate mature monolayers as previously reported (Wu et al., 2021), unless otherwise specified.

Primary human dermal fibroblasts (Lonza) were grown in DMEM - 4.5 g/L glucose (Thermo Fisher Scientific), 25 mM HEPES (Thermo Fisher Scientific), 100 μg/mL streptomycin, 100 U/mL penicillin (Thermo Fisher Scientific), and 10% FCS (Thermo Fisher Scientific). Primary human myoblasts (Cook MyoSite) from different age donors were grown in Skeletal Muscle Cell Growth Medium (C-23060, Promocell). All reported experiments were performed using cells with less than six passages in vitro, unless otherwise specified.

2.2. In vitro models of senescence and acute glucose treatment

To induce endothelial cell senescence in vitro, different methods were used. Glucose induced cell senescence: cells were seeded at an initial density of 8×10^3 cells/cm^2 and 24 h after seeding cells were treated with glucose (50 mM for HUVEC and retinal cells, 25 mM for HRGEC cells) every 2 days for 6 days (Prattichizzo et al., 2018). Control samples were obtained following the same culture scheme with full growth medium. Inflammatory senescence: 24 h after seeding, HUVEC cells were treated with TNF-α (10 ng/mL, #300–01 A, PeproTech, USA) every 2 days for 6 days (Khan et al., 2017). Control samples were obtained following the same culture scheme with full growth medium. Replicative senescence: HUVEC were cultured over time until they reached passage 15 (Wagner et al., 2001).

Acute glucose treatment was performed treating HUVEC with 50 mM glucose for 6 h (Haidari et al., 2014).

2.3. Gelatin-glutaraldehyde crosslinking

To enhance endothelial cell adhesion, all surfaces were coated with glutaraldehyde (Sigma-Aldrich)-crosslinked gelatin (#104070, Merck Millipore), as previously reported (Orsenigo et al., 2012). Briefly, the samples were incubated for 1 h at 37 °C with 1.5% gelatin followed by a crosslinking with 2% glutaraldehyde solution for 15 min at RT. The glutaraldehyde was then replaced by 70% ethanol. After 1 h at RT, 5 washes with PBS (Thermo Fisher Scientific) followed by overnight incubation with PBS containing 2 mM glycine were performed. Before cell seeding, slides were washed another 5 times with PBS.

2.4. Western blotting

Western blot analysis was performed according to standard protocols. Confluent monolayers of EC were lysed in boiling Laemmli sample buffer [(2% SDS, 20% glycerol, and 125 mM Tris-HCl (pH 6.8)]. Protein concentration was determined using a BCA Protein Assay kit (Thermo Fisher Scientific). Equal amounts of proteins were loaded on a gel, separated by SDS-PAGE and transferred to a nitrocellulose membrane (Thermo Fisher Scientific). After blocking and incubation with primary and horseradish peroxidase-linked secondary antibodies, specific bindings were detected using a chemiluminescence system (Thermo Fisher Scientific). Western blot bands were quantified using optic densitometry software (Image Lab 6.0.1, Biorad) and normalized to the levels of an appropriate housekeeping protein.

2.5. Co-Immunoprecipitation

Confluent monolayers of EC were solubilized in cold immunoprecipitation lysis buffer [20 mM HEPES (pH 7.5), 1.5 mM EDTA, 150 mM NaCl, 1.5 mM $MgCl_2$, 1% Triton X-100, 0.5% glycerol and protease/phosphatase inhibitors] and incubated on ice for 15 min. The protein lysate was then precleared with Protein A/G Sepharose beads (Thermo Fisher Scientific) for 2 h at + 4 °C. Subsequently, protein concentration was determined using a BCA Protein Assay kit, and equal amounts of protein were incubated with immune antibodies and captured by protein A/G Sepharose beads overnight at 4 °C. As a control, immune antibody was incubated with immunoprecipitation lysis buffer and protein A/G Sepharose beads overnight at 4 °C. The following day, beads were washed several times with immunoprecipitation lysis buffer and boiled in an appropriate volume of Laemmli sample buffer. Immunoprecipitated material was analyzed through standard western blot analysis.

2.6. Substrate preparation and flow experiments

To fabricate the substrates for flow experiments, a 126 × 70 mm^2 rectangle was cut from 120 μm-thick cyclic olefin copolymer (COC) foil (Ibidi). A patch with the dimensions of 30 mm × 15 mm was cut from the center of the substrate. The surfaces were cleaned with 70% ethanol, oxygen plasma treatment (80 W for 60 s, 1 ± 0.2 mbar) was performed to clean the substrates and increase their hydrophilicity, and finally the substrates were coated with glutaraldehyde cross-linked gelatin to increase cell adhesion. HUVEC were seeded at high initial density (450 cell/mm^2) and grown in static conditions for 72 h to generate mature

monolayers, as previously reported (Orsenigo et al., 2012). Flow experiments were performed in a custom-designed parallel plate flow chamber as previously described (Chala et al., 2021). The flow rate was selected to reach the target wall shear stress (WSS) value, in accordance with the following equation:

$$\tau = 6Q\mu/WH^2$$

where τ refers to the WSS, Q to the volumetric flow rate, μ to the dynamic viscosity of water at 37 °C, W to the width and H to the height of the chamber. Specifically, cells were conditioned for 18 h with a flow yielding a nominal WSS of 1.4 Pa. At the end of each experiment, the cells were fixed, and immunofluorescence staining performed.

2.7. Immunofluorescence

Cells were fixed with 4% paraformaldehyde, permeabilized for 10 min with PBS 0.5% Triton X-100 and incubated for 1 h at room temperature in a blocking solution of PBS with 2% BSA. Subsequently, samples were incubated with primary antibodies diluted in blocking buffer overnight at 4 °C, washed with PBS, followed by appropriate secondary antibody incubation for 1 h at room temperature. DAPI was used to counterstain nuclei.

2.8. Paracellular permeability assay

The assay was carried out as previously reported (Wang et al., 2019). Briefly, endothelial monolayers were cultured on biotin-conjugated 1.5% gelatin. At selected time points (3 days after compound treatment or 48 h after siRNA transfection) Oregon green 488-conjugated avidin (Thermofisher Scientific) was added to the culture medium at a final concentration of 25 μg/mL for 3 min. The medium was then removed, and ice-cold 100% methanol was used to fix the cells for 10 min. Residual unbound avidin was removed by washing samples with PBS after fixation. Immunofluorescence for VE-CADHERIN was performed to identify junctional discontinuities.

2.9. Senescence-associated beta-galactosidase staining

SA-β-gal activity was measured using a histochemical senescence detection kit (abcam) following the manufacturer's instructions. Briefly, samples were fixed with the fixative solution for 15 min at room temperature. Cells were then washed twice with PBS and incubated at 37 °C without CO2 supply in freshly prepared SA-β-gal staining solution. After overnight incubation, the reaction was stopped by removing the SA-β-gal staining solution and cells were washed twice with PBS. The percentage of SA-β-gal positive cells was determined by counting all SA-β-gal positive cells (blue cells) under bright field illumination. The total number of cells was determined with a DAPI counterstaining and subsequent fluorescence microscopy imaging.

2.10. Image acquisition

Confocal microscopy was performed at room temperature using an automated Nikon-Ti spinning disk confocal microscope (Nikon) equipped with an Andor DU-888 camera (Oxford Instruments) and a pE100 LED illumination system (CoolLED Ltd.) with violet (405-nm laser diode), blue (488 nm; Argon), yellow (561 nm; solid state) and red (633 nm; HeNe) excitation laser lines. Only adjustments of brightness and contrast were used in the preparation of the figures. For comparison purposes, different sample images of the same antigen were acquired under constant acquisition settings. Image acquisition was performed using a 63X/1.4 NA and 40X oil immersion objective (HCX PL APO 63 × Lbd BL, Leica). Fluorescent Z-stacks of the signals emitted were acquired selecting the optical filters based on the respective emission. ImageJ version 1.33 was used for data analysis.

2.11. Image analysis

2.11.1. Colocalization analysis

The junctional localization of pVE-CADHERIN, ZO1 and CLAUDIN-5 was evaluated through their colocalization with VE-CADHERIN protein. This analysis was performed using the cell tracking software Imaris (Bitplane Scientific Software). Immunofluorescence images were uploaded into Imaris and the Pearson's coefficient, an indicator of the colocalization, was computed.

2.11.2. VE-cadherin width analysis

Width of the VE-CADHERIN staining was manually calculated using ImageJ (National Institute of Health). First, the images were imported in the software, subsequently lines perpendicular to the border of the cells were drawn on the VE-CADHERIN signal using the "Freehand" tool. The length of the lines corresponding to the width of the VE-CADHERIN junctions was plotted using the "Measure" option.

2.11.3. Biotin-avidin analysis

The fraction of area per field of view covered by biotin-avidin was measured using ImageJ (National Institute of Health). The images showing the biotin-avidin signal were imported in the software. The "Measure" option was used to obtain the total area of the field of view. The "Automatic Threshold" tool and the "Measure" option were used to determine the area covered by the biotin-avidin signal. Finally, the fraction of biotin-avidin leakage was obtained by dividing the area covered by the biotin-avidin signal with the total area of the field of view.

2.11.4. Intensity profile VE-cadherin analysis

The intensity profile of the VE-CADHERIN signal was plotted using ImageJ (National Institute of Health). After the images with the VE-CADHERIN signal were imported in the software, a line parallel to the edge of the cell and crossing the middle of the VE-CADHERIN signal was drawn using the "Freehand" tool of ImageJ. The "Plot profile" option was selected and the intensity value per μm of the line was exported in an Excel file.

2.11.5. γ-H2AX foci quantification

The FoCo algorithm was used to analyze the images as previously reported (Lapytsko et al., 2015). The number of foci per nuclei was extracted ad cells were divided in subgroups based on the number of foci detected.

2.11.6. Cell and nuclei area and cell density analysis

The fluorescent images of the VE-CADHERIN signa, were used to determine the cell and nuclei area and the cell density. Images were imported in ImageJ and the cell and nuclei area was determined manually using the 'Freehand selection' tool. Cell density was determined by manually counting the number of cells per field of view using the 'Multi Point' tool.

2.11.7. Flow-induced orientation analysis

The fluorescent images of the VE-CADHERIN signal were used to determine the cell orientation. Each image was imported in ImageJ and the border of each cell was determined manually using the 'Freehand selection' tool so that the software could assign the best fit ellipse to the contour of each cell. The orientation of each cell was then defined by the absolute angle between the direction of the flow and major axis of the ellipse.

In static conditions, cells maintain randomly distributed alignment, therefore the mathematical average of measured orientation in the monolayer is close to 45°. Any deviation from this midpoint indicates a level of collective orientation. When cells are exposed to 1.4 WSS flow, they collectively align along its direction (Chala et al., 2021). This process is reflected by the decrease of the average alignment to values

closer to 0°.

2.12. Antibodies and reagents

The primary antibodies were: rabbit anti-VE-CADHERIN (Cell signaling, Netherlands, 1:100 IF, 1:1000 WB, #2500); mouse anti-CLAUDIN-5 Alexa Fluor 488 (Thermofisher Scientific, 1:100 IF, 1:1000 WB, #352588); rabbit anti-ki67 (abcam, 1:500 IF, #ab16667); mouse anti-γ-H2AX (abcam, 1:3500, IF, #ab11174); mouse anti-P16 (Santa Cruz, 1:1000 WB, #sc-56330); rabbit anti-NF-kB p65 (Thermo-Fisher Scientific, 1:1000, #510500,),mouse anti-ZO-1 Alexa fluor 647 (Thermofisher Scientific, 1:100 IF, 1:1000 WB, #MA3–39100-A647); rabbit anti p-Y658-VE-CADHERIN (1:10, custom made as reported by Orsenigo et al. (Orsenigo et al., 2012)); mouse anti-DYRK1B (Santa Cruz, 1:100 IF, 1:500 WB, #sc-390417); mouse anti-VINCULIN (Sigma-Aldrich, 1:2000 WB, #V9131); rabbit anti-Phosphoserine/threonine (Thermo Fisher Scientific, 1:500 WB, #PA5–121314); mouse anti-Phosphotyrosine (BD Biosciences, 1:1000 WB, #610000); mouse anti-p120 Catenin (BD Biosciences, 1:1000 WB, #610133); mouse anti-GAPDH (Santa Cruz, 1:1000 WB, #sc-47724); rabbit anti-AKT (Cell signaling, 1:1000 WB, #9271); rabbit anti-Phospho-AKT (threonine 308) (Cell signaling, 1:1000 WB, #9275). The secondary antibodies for immunofluorescence were: donkey anti-mouse Alexa Fluor 555 (1:200; #A31570) conjugated; donkey anti-mouse Alexa fluor 488 (1:200, #A21202) conjugated; and donkey anti-rabbit Alexa Fluor 555 (1:200, #A32794) conjugated from Thermo Fisher Scientific. Cell nuclei were counterstained by DAPI (1:1000, #62248) from Thermo Fisher Scientific. The secondary antibodies for western blot were anti-mouse IgG, HRP-linked (1:2000, #7076) and anti-rabbit IgG, HRP-linked (1:2000, #7074) from Thermo Fisher Scientific.

The cell-impermeant viability indicator Ethidium homodimer-1 (EthD-1) (4uM, #E1169 Thermo Fischer Scientific) was used for cell death analysis following the Manufacturer's instructions.

2.13. siRNA transfection

For siRNA transfection, cells were plated at a density of 0.6×10^5 cells/cm^2 in complete medium and transfected with either scrambled (*Scr*) siRNA (ON-TARGETplus Non-targeting Control Pool, D-001810–10–05; Horizon Discovery) or *DYRK1B* siRNA (ON-TARGETplus Human DYRK1B (9149) siRNA-SMARTpool, L-004806–00–0005; Horizon Discovery). Transfection was performed with RNAiMAX (Thermo fisher Scientific) in accordance with the manufacturer's instructions.

2.14. Plasmid transfection

To overexpress DYRK1B, a customized pRP[Exp]-mCherry-CMV>hDYRK1B[NM_004714.3] (Vector Builder) was transfected in control HUVEC cells. Transfection was performed with LipofectamineTM 3000 (#L3000–001, Thermo Fisher Scientific) in accordance with the manufacturer's instructions. The higher level of expression of DYRK1B after 24 h of transfection was verified by WB.

2.15. Gene expression analysis

Total RNA was isolated using a RNeasy Mini kit (Qiagen), and 500 ng total RNA was reverse transcribed with random hexamers (High-Capacity cDNA Archive Kits; Applied Biosystems), following the manufacturer's instructions. The cDNAs were amplified using the SYBR green gene expression assay (Thermo Fisher) and an ABI/Prism 7900 HT thermocycler. The primers used are: *DYRK1B* forward 5′-CAC ACG CAG GTA TTG CCT GAT-3′ and *DYRK1B* reverse 5′-GTC CAC AGA GAG CTT ACG CA-3′ (Fang et al., 2018); *GAPDH* forward 5′-AAG GTC GGA GTC AAC GGA TT-3′ and *GAPDH* reverse 5′-CTC CTG GAA GAT GGT GAT GG-3′ (Tanikawa et al., 2016); *IL6* forward 5′-GATTCAATGAGGAGACTTGCC-3′ and *IL6* reverse 5′-TGTTCTGGAGGTACTCTAGGT-3′ (Tsuji et al., 2020); *CDKN1A* (P21) forward 5′-ACATCGCCAAGGAAAAACGC-3′ and *CDKN1A* (P21) reverse 5′-GTCTGTTTCGGTACTGTCATCC-3′ (Sun et al., 2016). For the quantification of gene expression, the comparative Ct method was used. Briefly, the average of Ct values of the housekeeping genes was calculated and used as reference Ct (Ct-ref). For each gene of interest, we calculated the ΔCt as follows: ΔCt=Ct-gene−Ct-ref. Then, the data were expressed as $2^{-\Delta Ct}$ for each sample. Finally, for each experiment, we calculated the average of the $2^{-\Delta Ct}$ values of the samples of the control group, and we divided the value of each sample for this average. The resulting values were used for the plot and the statistical analysis (see dedicated section below).

2.16. Statistical analysis

The Shapiro-Wilk test was used to test the normality of the data. For normally distributed data, t-test was performed, while for non-normally distributed data, Mann-Whitney U test was performed. For all tests, a significance level of 0.05 was used. Bar plots depict the mean with error bars for the standard error of the mean SEM. In all box plots the population means are reported as a horizontal line inside the boxplot, the population medians are reported as a small square inside the box plot. The total number of events counted is reported in the figure caption. The number of independent experiments is indicated as n and the number of total cells/fields of view is shown as n′ (*$p < 0.05$, **$p < 0.01$, ***$p < 0.001$).

2.17. Artificial intelligence target prediction

Two methods were used to predict targets for the cellular senescence mechanism: 1) relational inference machine learning algorithm on top of the Benevolent Knowledge Graph (the Benevolent Platform™, (Paliwal et al., 2020)) and 2) causal reasoning algorithm to infer the regulators of tissue-specific aging signatures and differential expression between senescent and non-senescent cells derived from transcriptomics data. These methods were aggregated in a cell type specific manner, using the relevant tissue signatures for the cell type of interest. For disease mapping, the Benevolent Platform™ was used to suggest diseases and the cell types where the senescent mechanism is known to play a role. These suggestions were manually reviewed by expert biologists and clinicians to form a curated list of indications and corresponding cell types where senescence might play a role.

2.18. Compound treatments and IC_{50} determination

DYRK1B inhibition was performed using the AstraZeneca small molecules AZ-Dyrk1B-33 (Kettle et al., 2015) and AZ191 (Ashford et al., 2014). Both compounds were tested at the following concentrations: 10, 3, 1, 0.3, 0.1, 0.03, 0.01, 0.003 μM with an incubation time of 3 days. Briefly, glucose-treated kidney endothelial cells (DN model, see In vitro models of senescence and acute glucose treatment section) were seeded in 96 well plates at the density of 3×10^4 cells/well to have immediate confluent monolayers. After 3 days that allow junctional stabilization and monolayer maturation, cells were treated with the inhibitors and DMSO as negative control. After 3 days of treatment cells were fixed and the SA-β-gal activity assay was used as a readout. In details: SA-β-gal staining was followed by a nuclear staining (DAPI) to determine in each well the total number of cells, the total number of SA-β-gal- positive and SA-β-gal-negative cells. The individual IC_{50} concentrations for the SA-β-gal-positive cell clearance from senescent endothelial monolayers were obtained by fitting a four-parameter logistics curve to the datasets to produce a dose-response curve. An IC50 geometric mean and confidence intervals were then generated from the curve fit results from 3 biological repeats (Zhang et al., 2013).

Human myoblasts isolated from young and old donors were treated

with the inhibitors at 0.03 μM and DMSO as negative control. After 3 days of treatment cells were fixed and the SA-β-gal activity assay was measured.

2.19. KI-67 proliferation assay

Cell proliferation rate was quantitatively analyzed detecting KI-67 protein by immunofluorescence. Briefly endothelial cells were seeded on gelatin-coated glass coverslips in sparse condition (15×10^3 cells/cm^2). After 24 h samples were fixed with 4% paraformaldehyde and stained for KI-67 and DAPI.

3. Results

3.1. Artificial intelligence-driven drug target identification

The Benevolent Platform™ was leveraged to prioritize targets to test experimentally (Richardson et al., 2020; Sharma et al., 2020). The Platform uses a foundation of a disease-agnostic Knowledge Graph that integrates large quantities of diverse and independent biomedical data sources, including over 35 million scientific papers and the contents of dozens of structured databases, and a suite of machine learning models. These models extract interrelationships between biomedical concepts in the Knowledge Graph. The Knowledge Graph can be searched or explored using interactive tools, as well as novel proprietary algorithms as described (Paliwal et al., 2020).

Specifically, the Knowledge Graph was used as input to a tensor factorisation machine learning model (Paliwal et al., 2020) that ranks protein coding genes for a given disease or mechanism. Here, the model was used to prioritize genes that modulate cellular senescence. A second approach was used to prioritize genes as potential regulators of tissue specific signatures of aging. We enriched the Benevolent Knowledge Graph to better represent senescence related biological concepts and their respective relationships derived from both structured and unstructured data sources. In addition, transcriptomics datasets from senescent vs non senescent cells were integrated to describe the level of expression in endothelial cell types derived from the genotype tissue expression project (GTEx) (Consortium, 2013). From the list of possible predicted senolytic targets, the Benevolent Platform™ surfaced data from the Knowledge Graph allowing biologists to prioritize targets based on plausibility to moderate senescence biology, novelty for the indication, and expression in relevant cell types. Based on these assessments, DYRK1B was selected for experimental validation. The artificial intelligence driven target identification methods are depicted in (Fig S1 **a**).

3.2. Hyperglycemia triggers senescent phenotype in kidney- and retinal-derived endothelial cells

It has been previously reported that hyperglycemia in diabetes promotes cell senescence (Narasimhan, Flores et al., 2021). Indeed, we detected higher levels of senescence associated β-galactosidase (SA-β-gal) activity, a marker of cell senescence (Dimri, Lee et al., 1995; Kurz, Decary et al., 2000), in kidney endothelial cells obtained from patients with DN compared to those of healthy donors (Fig. S1 b, ~50% vs ~5%).

To investigate the role of cell senescence in diabetes, we generated in vitro model systems of DN and DR, by treating healthy endothelial monolayers of kidney or retina origin with glucose 25 mM or 50 mM, respectively, for 1 week as previously reported (Mortuza, Chen et al., 2013; Prattichizzo, De Nigris et al., 2018) (Fig. S1 c). Glucose-treated cells (DN and DR models) and cells from patient with DN showed typical senescence-associated features (Fig. S2) including increased SA-β-gal activity,P16 (INK4A) (Zhang, Wu et al., 2012), *CDKN1A* (P21) (Ock et al., 2020), histone γ-H2AX (DNA damage marker, (Bernadotte, Mikhelson et al., 2016)), NF-kB p65 and IL6 (SASP phenotype markers, (Coppe et al., 2010; Salminen et al., 2012; Zoico et al., 2021)) and reduced cell proliferation rate compared to the untreated control counterparts. Moreover, they showed an increase in nuclear and cellular size as well as a reduction in the local cell density. All these characteristics overall confirmed the induction of senescence in these cell populations.

3.3. Cell senescence is detrimental for the control of permeability and junctional integrity in endothelial cells

Impaired endothelial barrier functions are characteristic of diabetes and endothelial cell senescence (Kimura et al., 1993; Hadi and Suwaidi, 2007; Krouwer et al., 2012). Thus, we evaluated barrier integrity using a vascular permeability imaging assay (Wang, Chung et al., 2019). As shown in Fig. 1, endothelial monolayers of control cells presented a continuous and thick staining of VE-CADHERIN, the major component of adherens junctions (Dejana, 2004), which correlated with few and small paracellular focal sites of leakage. Conversely, DN and DR cells showed thinner and discontinuous VE-CADHERIN-positive junctions and a strong increase in paracellular avidin leak which suggests that VE-CADHERIN junctional integrity, as well as the overall organization of both adherens and tight junctions, are impaired.

We then characterized the junctional complexes in more detail. While control cells retained their ability to form mature monolayers, senescent cells did not. Indeed, by immunofluorescence and western blot, we found that cells obtained from a DN donor, as well as kidney and retina endothelial cells treated with glucose, showed a reduction both in VE-CADHERIN protein expression as well as in the width of the adherens junctions, compared to the untreated control samples (Fig. 2 a-e).

The tyrosine phosphorylation of the VE-CADHERIN complex is critical for the integrity of adherens junctions and the control of endothelial permeability. The evaluation of the level of phosphorylation of VE-CADHERIN at tyrosine residue 658, a marker of the opening of the endothelial junctions (Harris and Nelson, 2010; Orsenigo et al., 2012), revealed that in the DN and DR models VE-CADHERIN was significantly phosphorylated compared to control cells (Fig. 2 a, f).

Finally, the tight junction markers ZO-1 and CLAUDIN-5 showed an overall reduction in their expression a in the glucose-treated cells of DN and DR models and in the DN patient, and a reduction of junctional localization for ZO-1 in the DN model and for CLAUDIN-5 in the DR model, which is consistent with the impairment in the control of permeability (Fig. 3).

All these data demonstrate that the presence of senescent endothelial cells in a monolayer negatively impacts on the proper control of the barrier functions as well as on the integrity of adherens and tight junction complexes.

3.4. DYRK1B expression is increased in senescent endothelial cells

As previously reported, proteins of the DYRK family promote cell quiescence, survival, and senescence (Boni et al., 2020; Triana-Martinez et al., 2020).

We analyzed the expression of DYRK1A and DYRK1B in DN and DR model systems. As shown in Fig. 4 a and b, DYRK1A levels were strongly reduced in glucose treated DN cells compared to control, while no difference in DYRK1A expression was found in the DR model. Interestingly, DYRK1B expression was significantly upregulated in the senescent populations of both DN and DR cells (Fig. 4a, c and e), alongside the phosphorylation and activation of AKT (Fig. 4a, d), a downstream target of DYRK proteins (Abekhoukh et al., 2013). To broaden these observations, we verified that DYRK1B level was also increased in other models of in vitro-induced cell senescence, besides the one associated with diabetes. HUVEC cells, in which cell senescence was induced by different triggers such as treatments with TNF-α (Khan et al., 2017), glucose (Prattichizzo et al., 2018), or by passage number (p15, replicative senescence) (Jong et al., 2013), expressed higher levels of DYRK1B compared to the control counterpart (Fig. S3 a), as well as they

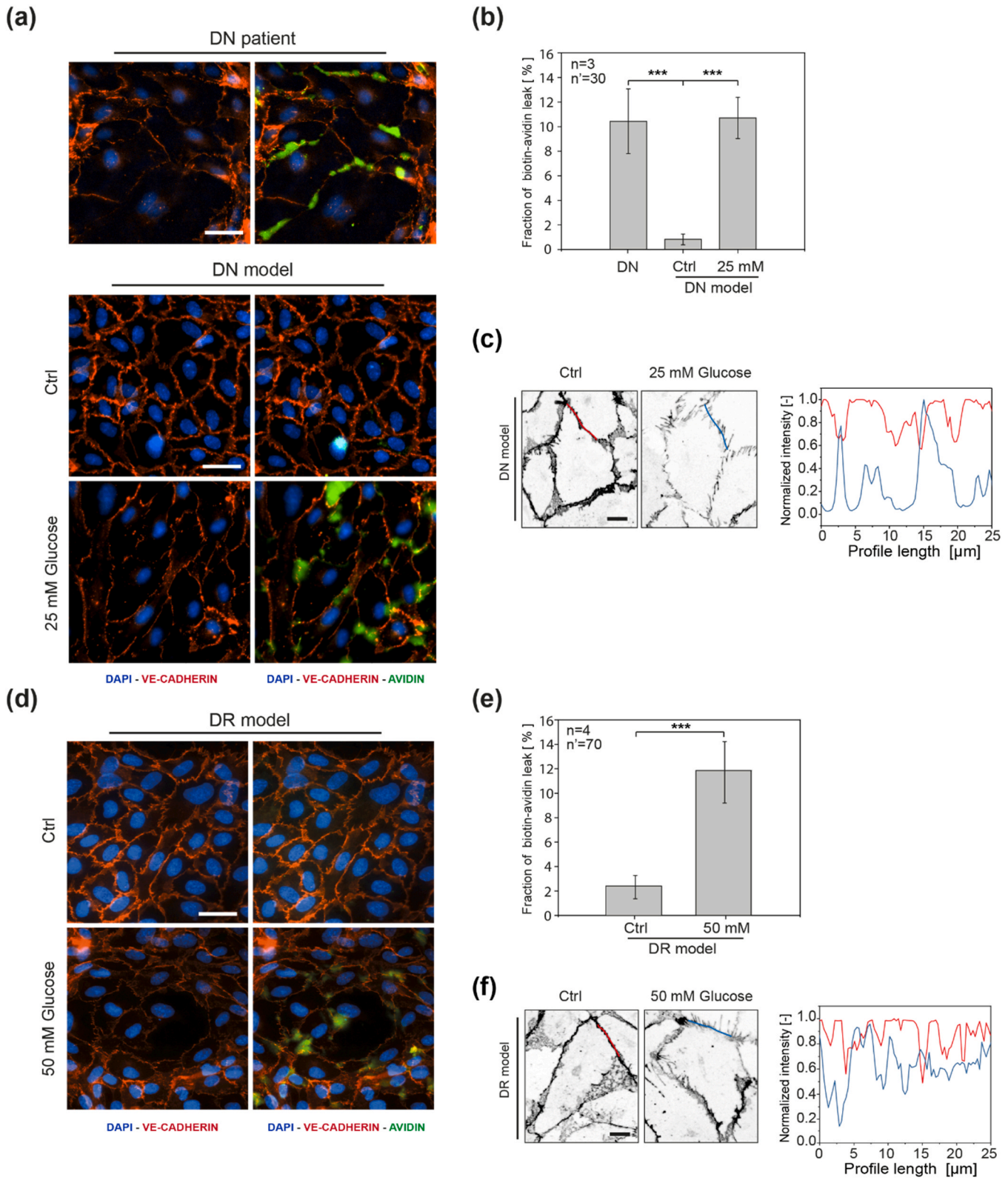

Fig. 1. Permeability analysis in senescent models of endothelial cell monolayer. (a) VE-CADHERIN (left) and VE-CADHERIN-AVIDIN (right) immunofluorescent staining of DN cell monolayers. (b) Biotin-avidin assay respective quantification for DN cells. (c) Inverted VE-CADHERIN immunofluorescent staining for treated (25 mM) and control DN cells and respective profile intensity plot. (d) VE-CADHERIN (left) and VE-CADHERIN-AVIDIN (right) immunofluorescent staining of DR cell monolayers. (e) Biotin-avidin assay respective quantification for DR cells. (f) Inverted VE-CADHERIN immunofluorescence staining for treated (50 mM) and control DR cells and respective profile intensity plot. n = number of independent experiments, n′= number of analyzed fields of view. Error bars correspond to the measured standard error of the mean, * **$p < 0.001$. Scale bar is 20 μm.

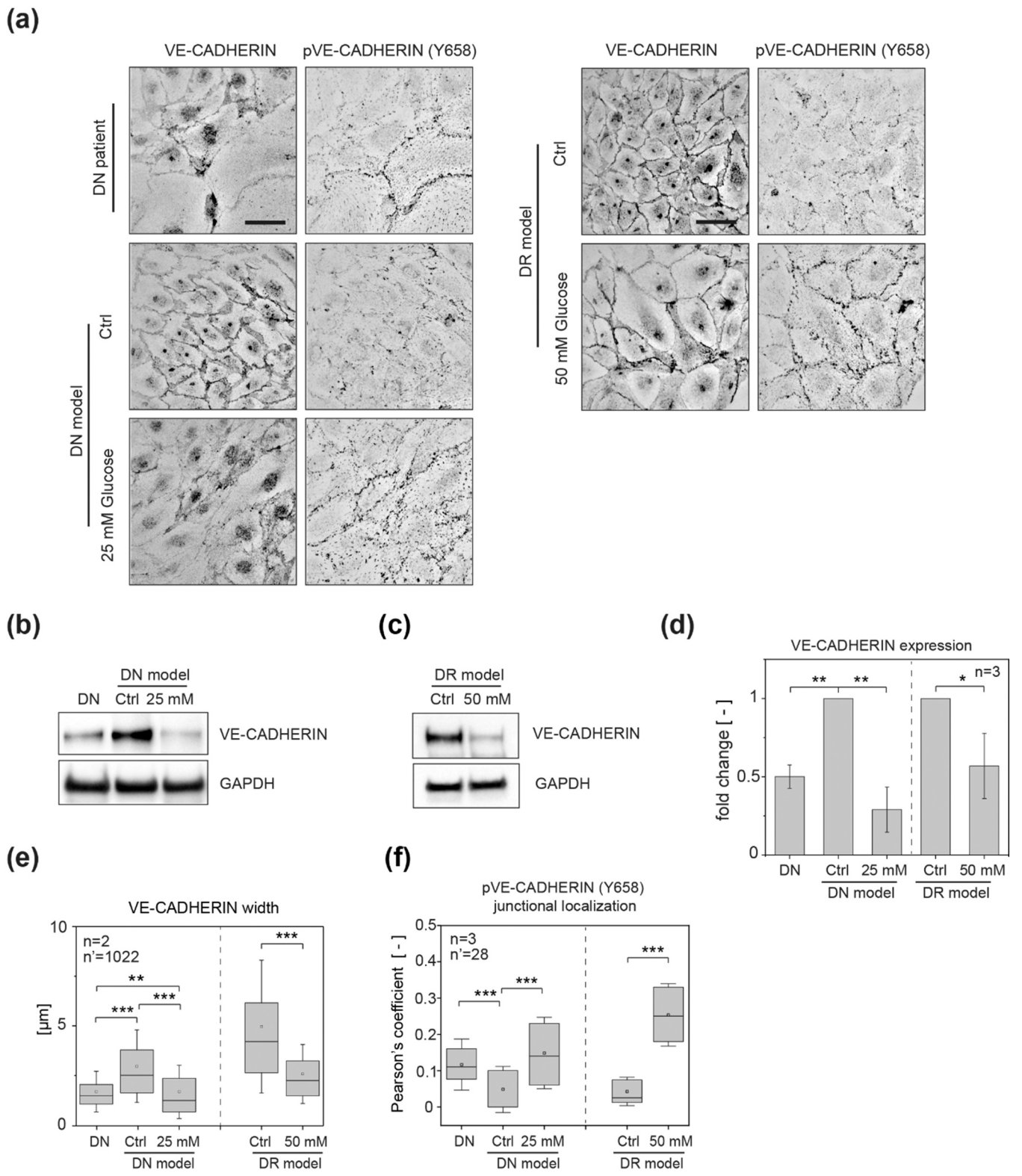

Fig. 2. Junctional integrity impairment in senescent models of endothelial cell monolayer. (a, b) Representative inverted VE-CADHERIN and pVE-CADHERIN (Y658) immunofluorescent staining of DN patient, and DN and DR cell monolayers. (b-d) Western blot (WB) analysis of VE-CADHERIN for DN patient, DN and DR models and relative quantification. (e) VE-CADHERIN junctional width analysis for DN patient, DN and DR models. (f) Colocalization analysis between VE-CADHERIN and pVE-CADHERIN (Y658). n = number of independent experiments, n′= number of analyzed fields of view. Error bars correspond to the measured standard error of the mean, *$p < 0.05$, * *$p < 0.01$, * **$p < 0.001$. Scale bar is 20 µm.

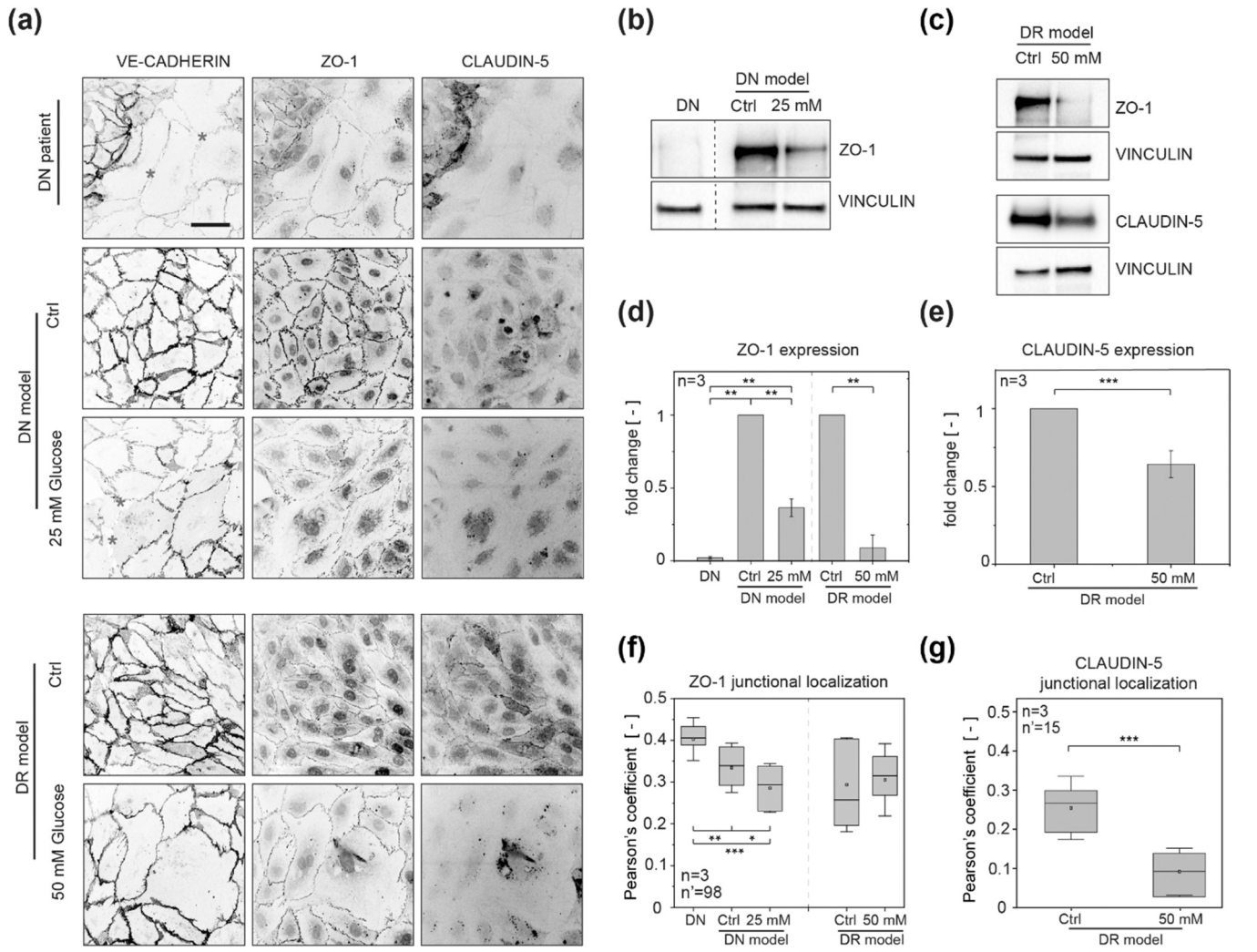

Fig. 3. Junctional integrity impairment in senescent models of endothelial cell monolayer. (a, b) Representative inverted VE-CADHERIN, ZO-1, and CLAUDIN-5 immunofluorescent staining of DN and DR cell monolayers. (b-e) WB analysis of ZO-1, and CLAUDIN-5 for DN patient, DN and DR models and relative quantification. (f, g) Colocalization analysis between VE-CADHERIN and ZO-1, and between VE-CADHERIN and CLAUDIN-5. n = number of independent experiments, n′= number of analyzed fields of view. Error bars correspond to the measured standard error of the mean, *p < 0.05, * *p < 0.01, * **p < 0.001. Scale bar is 20 μm.

display some features of cell senescence such as increased expression of P16 (INK4A) and NK-kB p65 (Fig. S3 a), increased cell and nuclear size and decreased local cell density (Fig. S3 b). By immunofluorescence analysis, we found that, besides the nuclear localization, a strong signal for DYRK1B was also present at the cell-cell contacts of senescent HUVEC cells (Fig. S3 c), thus suggesting a direct role in the alteration of the junctional complexes. As we previously reported for the DN and DR models, senescent HUVEC also presented thinner VE-cadherin-positive junctions which correlated with an impairment in the barrier functions (Fig. S3 d). Ultimately, we found that the increase of DYRK1B in senescent cells was not restricted to the endothelial cell type and to the human species. As shown in Fig. S4, higher levels of DYRK1B were detected in a model of replicative senescence of human fibroblasts (panel a), in human myoblasts isolated from old donors (panel b), and in glucose-treated aortic endothelial cells of bovine origin (panel c), suggesting that it can be considered a new general senescent marker.

All these data support the hypothesis that the increase of DYRK1B in senescent endothelial cells contributes to the deregulation of monolayer structure and functions.

3.5. *DYRK1B inhibition exerts senolytic effects on cells*

To determine the specific effects of DYRK1B inhibition on senescent cells in vitro, the senescent-induced DN cells were treated with increasing concentrations (0.003–10 μM) of AZ191 (Ashford et al., 2014) or AZ-DYRK1B-33 (Kettle et al., 2015), 2 reportedly selective and commercially available inhibitors of DYRK1B for 72 h. The cells were then subsequently fixed and stained for DAPI and SA-β-gal to detect total, senescent, and non-senescent (healthy) cell populations within the same well. Both compounds showed a reproducible senolytic effect, decreasing the senescent cell population (SA-β-gal positive) but not the healthy cell population (SA-β-gal negative) (Fig. S5 a). There was a dose-dependent decrease in senescent cell number with AZ191 (IC50 = 70 nM) and AZ-DYRK1B-33 (IC50 = 76 nM). In both cases there is a trend for an increase in the number of healthy cells, possibly due to these cells re-populating the monoculture as the senescent cells are lost. To confirm this observation, we verified the senolytic effect of DYRK1B inactivation upon its inhibition and knock-down (KD) in senescent cells measuring the percentage of cell death and cell proliferation. As shown in Fig. S5 b, AZ-Dyrk1B-33 treatments increased the percentage of dead cells over time, as well as the percentage KI-67 positive-cells in cell populations. 48 h after *DYRK1B* knock-down a trend of increase in the percentage of dead cells was observed compared to the *scramble (Scr)* control, while no difference in KI-67 positive-cells was detected. This is in line with previous observations showing that reduction or inhibition of DYRK1B triggered the apoptosis of quiescent cancer cells expressing

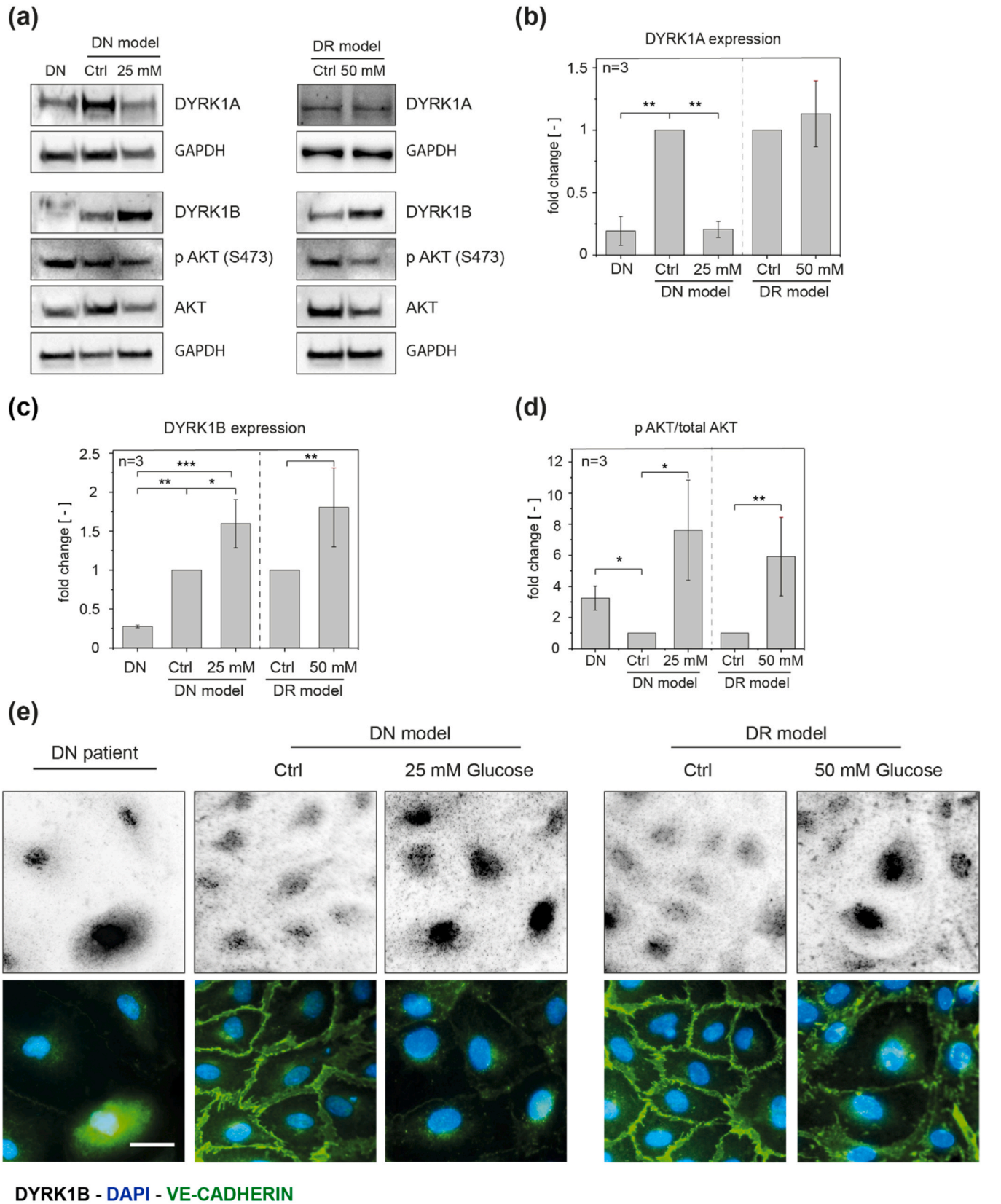

Fig. 4. DYRK1 expression is increased in senescent endothelial cell monolayer. (a-d) WB analysis of DYRK1A, DYRK1B, AKT, and p-AKT (S473) for DN patient (DN), DN and DR models and relative quantification. n = number of independent experiments. (e) Representative VE-CADHERIN and inverted DYRK1B immunofluorescent staining of DN and DR cell monolayers. Error bars correspond to the measured standard error of the mean, *$p < 0.05$, * *$p < 0.01$, * **$p < 0.001$. Scale bar is 10 μm.

high level of DYRK1B and the cell cycle re-entry (Becker, 2018).

The available DYRK1 compounds are also likely to inhibit the closely related kinases CLK1/4 (Lee Walmsley, Murray et al., 2021; Lindberg and Meijer, 2021). We thus verified by WB the expression of the potential off-targets. As for DYRK1A (Fig. 4 a, b), that the levels of CLK1 and CLK4 were not modified upon senescence induction (Fig. S5 c). Of note, it was extensively reported that inhibition of CLKs reduced cell proliferation (Muraki et al., 2004; Fedorov et al., 2011; Araki et al., 2015; Dominguez et al., 2016; Sako et al., 2017; Uzor et al., 2021), which is in contrast with our results. These data suggest that the observed effect is not driven by CLK inhibition but rather to that of DYRK1B. Last, the 2 inhibitors were tested on primary human myoblasts from donors of different ages. As shown in Fig. S5 d, also in this cell model DYRK1B inhibition was reducing the number of SA-β-gal-positive cells, suggesting that the senolytic targeting of DYRK1B is not restricted to endothelial cells.

3.6. DYRK1B inactivation restores endothelial barrier functions

We then analyzed the effect of small molecule inhibitors of DYRK1B kinase activity or *DYRK1B* siRNA KD on endothelial barrier functions. DN and DR endothelial monolayers were treated with AZ191 or AZ-DYRK1B-33 at 3 different concentrations, based on the previous results (Fig. S5 a). Indeed, the leak of permeability of DN and DR endothelial monolayers was significantly counteracted by the treatments with both AZ191 or AZ-DYRK1B-33 senolytic drugs targeting DYRK1B function (Fig. 5). These analyses were also extended to HUVEC senescent models obtaining similar results: DYRK1B inhibition partially rescued the barrier functions (Fig. S6). All these data strongly suggested that the increase of DYRK1B expression in senescent cells was detrimental for the proper organization and function of endothelial cell-cell junctions.

To confirm that the senolytic effect of the compounds is driven by DYRK1B inhibition, and not by the possible off-targets, we applied *DYRK1B* siRNA-mediated knock-down on DN and DR cell models. Similar results were obtained when senescent-induced cells were transfected with *DYRK1B* siRNA compared to *Scr* siRNA as control. The effective reduction of DYRK1B expression was verified 48 h after transfection by qRT-PCR and Western blot (Fig. 6 a- f), and barrier functions were evaluated. Interestingly, upon *DYRK1B* depletion, the permeability of senescent DN and DR endothelial cells was significantly reduced compared to the relative controls (Fig. 6g). We further confirmed this observation in HUVEC senescence models (Fig. S7). Of note, the knockdown resulted in loss of DYRK1B from endothelial cell–cell junctions (Fig. S7 a) and in a partial rescue of the barrier properties typically lost in senescent endothelial monolayers (Fig. S7 b and c).

3.7. DYRK1B inactivation restores mechanotransduction responses to wall shear stress stimulation

To make these observations even more convincing, we evaluated endothelial cell orientation under physiological wall shear stress (WSS), a collective cell response in which cell contacts play a key role (Tzima et al., 2005). Control, senescent (glucose-treated), and senescent HUVEC cells treated with AZ-DYRK1B-33 were exposed to a steady-state, laminar flow yielding a WSS of 1.4 Pa for 16 h (Chala et al., 2021), and the orientation of the cells at the end point of the flow stimulation was compared to that of the same cells cultured in static condition (Fig. S8). As previously reported (Chala et al., 2021), control cells under 1.4 WSS re-orient along the flow direction, while the senescent (glucose-treated) endothelial cells failed to do so. Interestingly, a strong rescue in cell orientation was observed in the senescent monolayers treated with the senolytic AZ-DYRK1B-33, further confirming that DYRK1B activity contributed to endothelial cell senescence through junctional dysfunction.

3.8. DYRK1B is a new component of the adherens junction complex

All the data presented here strongly suggest that DYRK1B could act directly at cell-cell contacts, contributing to the dismantling of endothelial junctions in senescent cells. To test this hypothesis, we performed co-immunoprecipitation assays coupled with western blotting. As shown in Fig. S9 panel a, immunoprecipitation of DYRK1B from total cell lysate of control and glucose-treated HUVEC detected an interaction between DYRK1B, p120-CATENIN and VE-CADHERIN, demonstrating that they were part of the same protein complex. Of interest, upon glucose treatment the interaction between DYRK1B and p120-CATENIN was increased, while that between p120-CATENIN and VE-CADHERIN was reduced. It was previously reported that the stability of VE-cadherin at cell junctions is potentiated by its binding with p120-CATENIN (Potter et al., 2005), and that serine/threonine phosphorylation of p120-CATENIN was acting as a negative regulator of cadherin adhesion (Aono et al., 1999). Given that DYRK1B has a serine/threonine kinase activity (Soppa and Becker, 2015; Boni et al., 2020), we wondered whether its increased interaction with p120-CATENIN was associated with a different level of serine/threonine phosphorylation of the latter. Interestingly, immunoprecipitation indicated that Serine and Threonine phosphorylation of p120-CATENIN, which mediates junction disassembly (Aono et al., 1999), was higher in the glucose-treated samples compared to the control cells (Fig. S9, panel b). All these results are in line with a potential direct role of DYRK1B in contributing to the phosphorylation and dismantling of the junction complexes in senescent endothelial cells, which leads to the barrier dysfunctions that occur during cell aging. We then asked if the overexpression of DYRK1B was solely sufficient to recapitulate the phenotypes observed in terms of endothelial barrier function regulation and its relationship with cell senescence. We thus transfected control HUVEC with a plasmid containing the human sequence of DYRK1B. WB of transfected cells confirmed the overexpression (Fig. S9 c). Of interest, immunofluorescence analysis revealed that the overexpressed DYRK1B was localized at cell-cell contacts (Fig. S9 d). As shown in Fig. S9 e, upon DYRK1B overexpression, which was much higher compared to the increase induced by cell senescence, only an increase in P16 (INK4A) was detected, in line with its well-established role in promoting cell cycle arrest (Becker, 2018), while no effect on NF-kB p65 expression was detected. Eventually, a slight although significant increase in permeability was detected in DYRK1B overexpressing cells, but still of lesser magnitude than that induced by cell senescence. Taken together, these results suggest that DYRK1B has a direct role in the destabilization of the adherens junctions, but it is not solely sufficient to induce the senescent-associated phenotypes, being rather a contributing factor.

4. Discussion

Cell senescence is a phenotype of normal cells characterized by permanent cell cycle arrest in response to various stimuli of different origin. Senescence of vascular beds reported in vivo indicates its involvement in the development of age-related pathological conditions characterized by vascular dysfunctions (Katsuumi, Shimizu et al., 2018). In diabetic disease, oxidative stress has been implicated as a major driver of hyperglycemia-induced endothelial dysfunctions (Hadi and Suwaidi, 2007), and endothelial cell senescence SA-β-gal functional kidney decline in DN patients (Verzola et al., 2008; Sturmlechner et al., 2017) in which senescence increases with the severity of the disease (Verzola et al., 2008). Specifically, senescent endothelial cell SASP and rarefaction are critical drivers of kidney fibrosis (Vasko et al., 2014; Kida et al., 2016). Similarly, hyperglycemia results in the loss of barrier integrity in retinal endothelial cells and increase in SASP in the vitreous fluids of DR patients (Oubaha et al., 2016). Interestingly, it has been reported for the first time that senolytic drugs decreased senescent cells in patients with DN (Hickson et al., 2019).

All this evidence prompted our interest at identifying new targets to

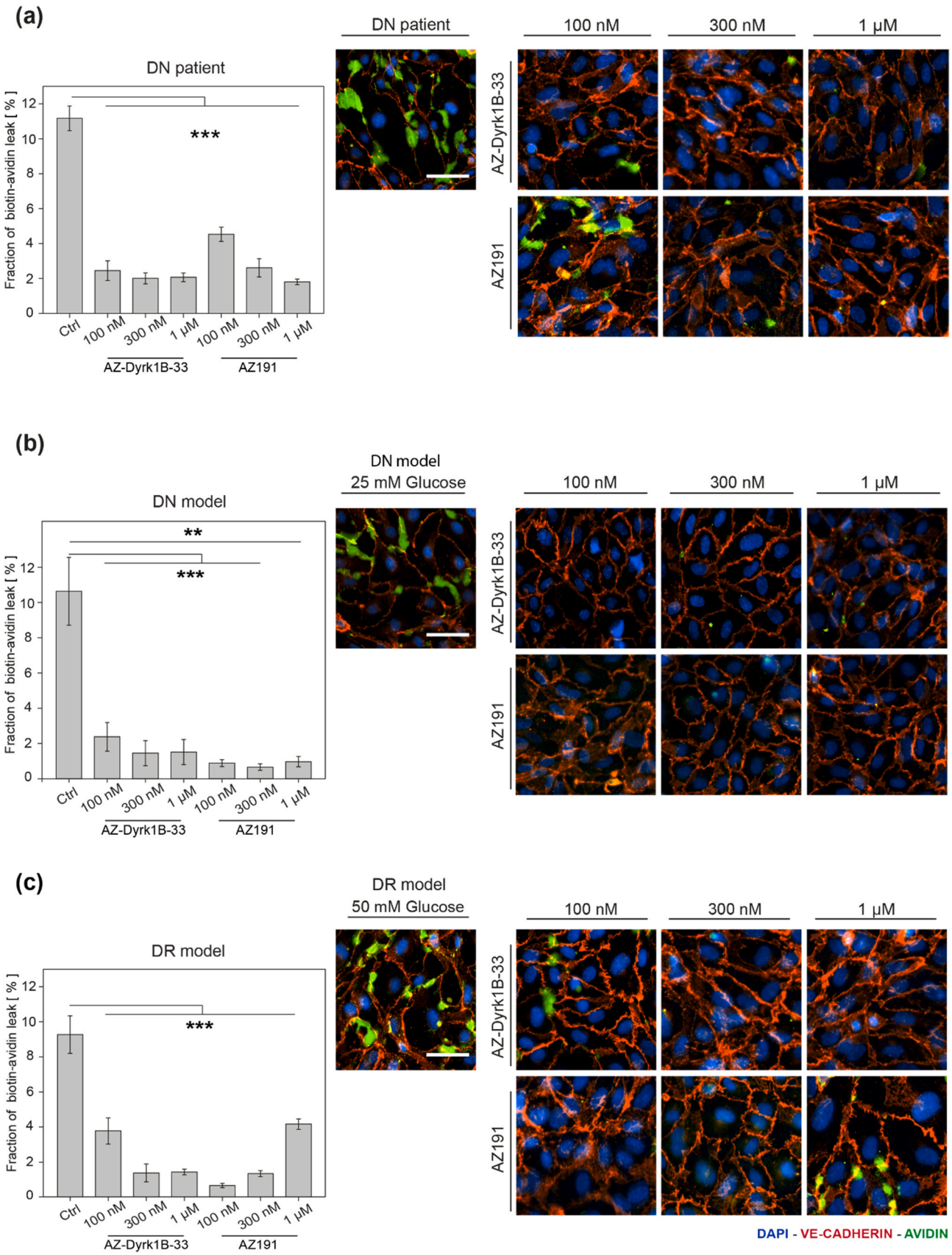

Fig. 5. DYRK1 inhibition and permeability assay in endothelial cell monolayer. (a-c) VE-CADHERIN and AVIDIN immunofluorescent staining of DN and DR cell monolayers upon DYRK1B inhibition to detect endothelial cell monolayer permeability and quantification. Scale bar is 20 µm. n = 3 independent experiments, n′= 168 no. of analyzed fields of view, * *p < 0.01, * **p < 0.001.

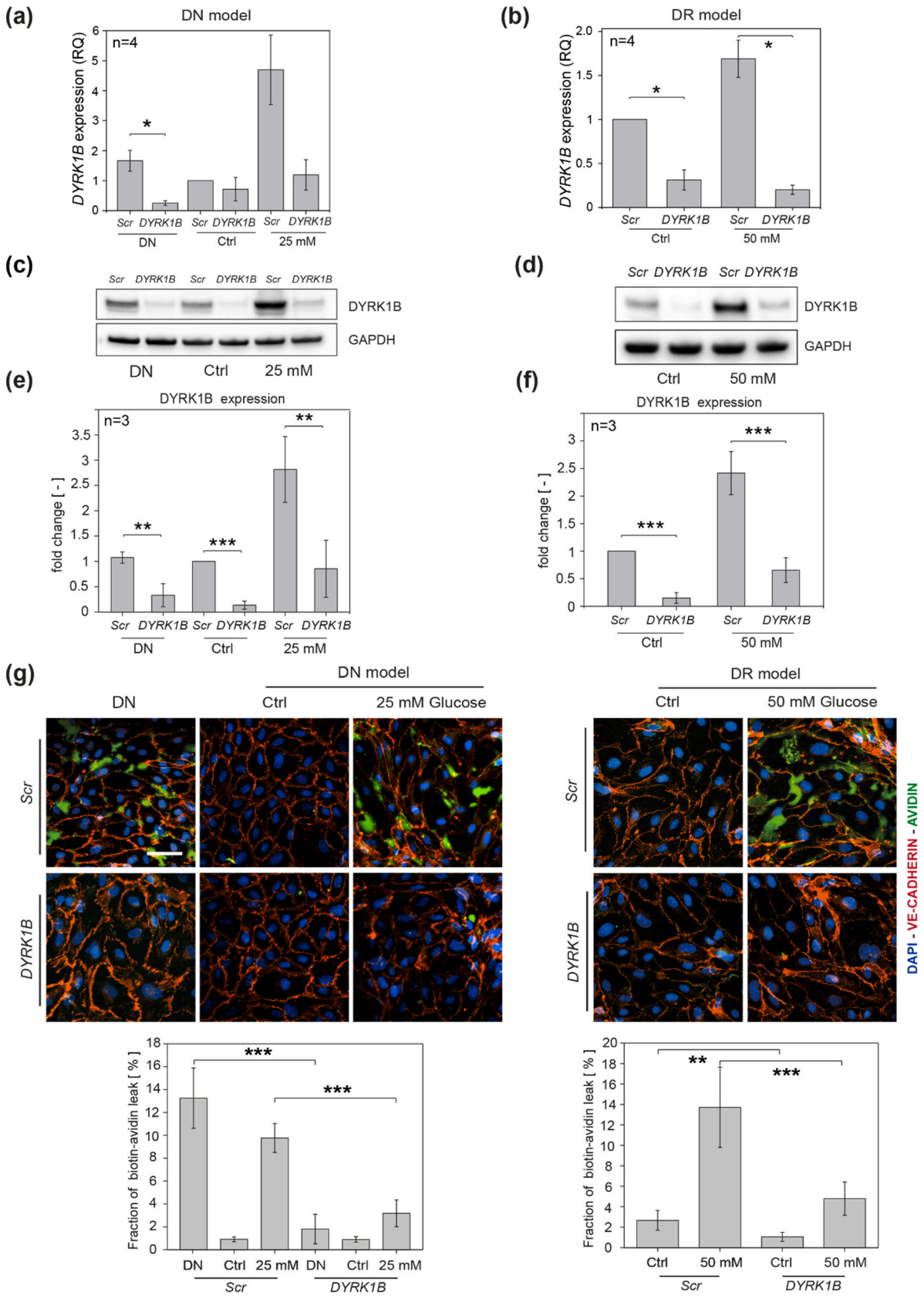

Fig. 6. DYRK1 knock-down and relative expression in endothelial cell monolayers. (a-b) RT-qPCR analysis of *DYRK1B* for DN patient, DN and DR models upon *DYRK1B* knockdown, n = 4 independent experiments, *p < 0.05. (c-f) WB of DYRK1B for DN and DR models upon *DYRK1B* knockdown and relative quantification; (e-f) n = 3. (g) VE-CADHERIN and AVIDIN immunofluorescent staining of DN and DR cells monolayers upon *DYRK1B* knockdown to detect endothelial cell monolayer permeability. Quantification of the fraction of biotin-avidin leak values is reported in the graph below. Scale bar is 20 μm. n = 3 independent experiments, n′= 104 no. of analyzed fields of view, *p < 0.05, * *p < 0.01; * **p < 0.001.

specifically clear senescent cell populations to ameliorate diabetic diseases. Using an artificial intelligence approach applied to target identification, we predicted that inhibition of the protein DYRK1B, would induce apoptosis in senescent endothelial cells. DYRK1B is overexpressed in a subset of cancers and induces cellular quiescence by blocking cells in the G_0 phase (Gao et al., 2013) and it sustains cell survival upregulating antioxidant genes (Lee et al., 2000). Moreover, previous reports show that both inhibition and depletion of DYRK1B increased cell apoptosis (Hu and Friedman, 2010; Ewton et al., 2011) and reduced cell cycle arrest (Ewton et al., 2011). Of interest, inhibition or depletion of DYRK1B showed a selective effect on cancer cells, expressing elevated levels of DYRK1B, and not on normal cells and tissues (Hu and Friedman, 2010; Ewton et al., 2011).

In this proof-of-concept study we show that DYRK1B is a valid new target for senescent cell clearing, as upon its inhibition or removal senescent endothelial monolayers recovered their impaired barrier properties and responses to mechanical stimuli.

Here we report that replicative and stress-induced (with high doses TNF-α or glucose chronic treatments) in vitro models of premature senescence of different cell types, as well as cells derived from old donors, identified by typical senescence-associated features (Salminen et al., 2012; Zhang et al., 2012; Gonzalez-Gualda et al., 2021; Zoico et al., 2021), displayed higher levels of DYRK1B, although to different extents, compared to their not-senescent or young counterparts. This observation was further confirmed by comparing senescence phenotypes and DYRK1B expression in endothelial cells isolated from healthy and diabetic patients.

Using all these model systems, we showed that the presence of senescent cells in endothelial monolayers impaired the expression and correct localization of proteins belonging to the adherens and tight junction complexes (Krouwer et al., 2012). Interestingly, we showed here for the first time that upon the increase of expression, besides the well-described nuclear localization (Abu Jhaisha et al., 2017; Dong et al., 2020), DYRK1B localized at the cell-to-cell contacts of senescent endothelial cells. Moreover, we demonstrated that DYRK1B was a component of the adherens junction complexes, since it co-immunoprecipitated with p120-CATENIN and VE-CADHERIN, and that senescent endothelial cells had increased levels of serine/threonine phosphorylated p120-CATENIN, which has been shown to weaken the junctions (Aono, Nakagawa et al., 1999). This might be linked to the Serine/Threonine kinase activity of DYRK1B.

The structural integrity of endothelial junctions ensures homeostasis in many types of collective cell behavior including tissue barrier functions (Dejana, 2004; Harris and Nelson, 2010), and transmits important intracellular signaling essential for flow-induced alignment (Tzima, Irani-Tehrani et al., 2005). We thus verified that, as previously reported, the barrier function of senescent monolayers was compromised (Krouwer, Hekking et al., 2012), as well as the collective response to flow (Chala, Moimas et al., 2021). Indeed, we showed here that the presence of senescent cells increased endothelial permeability to the small molecule avidin and impaired the coordinated reorientation of the cells along the direction of flow. All these observations prompt us to hypothesize that DYRK1B increased expression in senescent endothelial cells could have detrimental effects on junction organization and function, thus compromising proper endothelial collective responses.

To prove this, we used 2 potent commercially available DYRK1B kinase inhibitors and we first verified their senolytic ability to specifically kill SA-β-gal-positive cells from senescent endothelial monolayers, and we excluded possible off target contributions. We also showed that DYRK1B could be considered a new general senolytic target, as its inhibition reduced the number of SA-β-gal-positive cells in senescent myoblast populations. We then moved to determine whether the inhibition of DYRK1B could rescue some endothelial features compromised by senescence, such as paracellular permeability and cell reorientation under flow, which are both collective properties acting through the correct junctional complex organization. Treatments with both tested compounds partially decreased the permeability of the endothelial monolayers compared to the senescent untreated counterparts, in a dose dependent manner. Furthermore, the senolytic treatments fully rescued the impaired alignment in the direction of laminar flow triggered by cell senescence. To corroborate these results, we knocked-down *DYRK1B* in retinal, kidney and HUVEC models of cell senescence and this restored the impaired barrier properties.

Overall, the data presented here identified for the first time a role for DYRK1B in sustaining cell senescence and directly impairing junctional organization of endothelial monolayers. Moreover, DYRK1B inhibition effectively cleared senescent cells and restored monolayer properties.

CRediT authorship contribution statement

Francesca M. Pramotton: Performed the experiments, Collected the data, Analyzed the data, Prepared the figures, Contributed to the manuscript drafting. **Chantelle Hudson:** Contributed to conceiving the research and analyzing the data, Provided the materials, Wrote the manuscript. **Asra Abukar:** Performed the experiments, Collected the data, Analyzed the data, Contributed to the revision drafting. **James Dunbar:** Led the AI target prediction methods. **Andrew Potterton:** Performed the computational analysis. **Simone Tonnicchia:** Helped with data quantification. **Andrea Taddei:** Contributed to target identification and scientific discussion. **Edoardo Mazza:** Contributed with scientific discussion and critical reading of the manuscript. **Costanza Giampietro:** Conceived and supervised the research, Interpreted the data, Prepared the figures, Wrote the manuscript. All authors reviewed and approved the final manuscript.

Conflict of interest statement

The authors C.H., J.D., A.P. and A.T. are employees of BenevolentAI. The authors F.M.P., A.A., S.T., E.M. and C.G. declare no conflict of interests.

Data availability

Data will be made available on request.

Acknowledgments

We thank Sarah Seton-Rogers for proofreading the manuscript, the Benevolent target ID product and technology team Charlie Whicher, Dane Corneil, Daniel Neil, Delphine Rolando, Gabi Griffin, Kirill Shkura, and Neal Lewis who contributed to the artificial intelligence methods used to predict targets for the cellular senescence mechanism, and Josep Monserrat for sharing myoblast cells. This work was supported by the Swiss National Science Foundation (grant SNF; 205321_188828 to C.G.).

Appendix A. Supporting information

Supplementary data associated with this article can be found in the online version at doi:10.1016/j.mad.2023.111836.

References

Abekhoukh, S., Planque, C., Ripoll, C., Urbaniak, P., Paul, J.L., Delabar, J.M., Janel, N., 2013. Dyrk1A, a serine/threonine kinase, is involved in ERK and Akt activation in the brain of hyperhomocysteinemic mice. Mol. Neurobiol. 47 (1), 105–116.

Abu Jhaisha, S., Widowati, E.W., Kii, I., Sonamoto, R., Knapp, S., Papadopoulos, C., Becker, W., 2017. DYRK1B mutations associated with metabolic syndrome impair the chaperone-dependent maturation of the kinase domain. Sci. Rep. 7 (1), 6420.

Aono, S., Nakagawa, S., Reynolds, A.B., Takeichi, M., 1999. p120(ctn) acts as an inhibitory regulator of cadherin function in colon carcinoma cells. J. Cell Biol. 145 (3), 551–562.

Araki, S., Dairiki, R., Nakayama, Y., Murai, A., Miyashita, R., Iwatani, M., Nomura, T., Nakanishi, O., 2015. Inhibitors of CLK protein kinases suppress cell growth and induce apoptosis by modulating pre-mRNA splicing. PLoS One 10 (1), e0116929.

Aranda, S., Laguna, A., de la Luna, S., 2011. DYRK family of protein kinases: evolutionary relationships, biochemical properties, and functional roles. FASEB J. 25 (2), 449–462.
Ashford, A.L., Oxley, D., Kettle, J., Hudson, K., Guichard, S., Cook, S.J., Lochhead, P.A., 2014. A novel DYRK1B inhibitor AZ191 demonstrates that DYRK1B acts independently of GSK3beta to phosphorylate cyclin D1 at Thr(286), not Thr(288). Biochem J. 457 (1), 43–56.
Baker, D.J., Wijshake, T., Tchkonia, T., LeBrasseur, N.K., Childs, B.G., van de Sluis, B., Kirkland, J.L., van Deursen, J.M., 2011. Clearance of p16Ink4a-positive senescent cells delays ageing-associated disorders. Nature 479 (7372), 232–236.
Beck, J., Horikawa, I., Harris, C., 2020. Cellular senescence: mechanisms, morphology, and mouse models. Vet. Pathol. 57 (6), 747–757.
Becker, W., 2018. A wake-up call to quiescent cancer cells - potential use of DYRK1B inhibitors in cancer therapy. FEBS J. 285 (7), 1203–1211.
Bernadotte, A., Mikhelson, V.M., Spivak, I.M., 2016. Markers of cellular senescence. Telomere shortening as a marker of cellular senescence. Aging (Albany NY) 8 (1), 3–11.
Boni, J., Rubio-Perez, C., Lopez-Bigas, N., Fillat, C., de la Luna, S., 2020. The DYRK family of kinases in cancer: molecular functions and therapeutic opportunities. Cancers (Basel) 12 (8).
Chala, N., Moimas, S., Giampietro, C., Zhang, X., Zambelli, T., Exarchos, V., Nazari-Shafti, T.Z., Poulikakos, D., Ferrari, A., 2021. Mechanical fingerprint of senescence in endothelial cells. Nano Lett. 21 (12), 4911–4920.
Consortium, G.T., 2013. The Genotype-Tissue Expression (GTEx) project. Nat. Genet 45 (6), 580–585.
Coppe, J.P., Desprez, P.Y., Krtolica, A., Campisi, J., 2010. The senescence-associated secretory phenotype: the dark side of tumor suppression. Annu Rev. Pathol. 5, 99–118.
Dejana, E., 2004. Endothelial cell-cell junctions: happy together. Nat. Rev. Mol. Cell Biol. 5 (4), 261–270.
Dimri, G.P., Lee, X., Basile, G., Acosta, M., Scott, G., Roskelley, C., Medrano, E.E., Linskens, M., Rubelj, I., Pereira-Smith, O., et al., 1995. A biomarker that identifies senescent human cells in culture and in aging skin in vivo. Proc. Natl. Acad. Sci. USA 92 (20), 9363–9367.
Dominguez, D., Tsai, Y.H., Weatheritt, R., Wang, Y., Blencowe, B.J., Wang, Z., 2016. An extensive program of periodic alternative splicing linked to cell cycle progression. Elife 5.
Dong, C., West, K.L., Tan, X.Y., Li, J., Ishibashi, T., Yu, C.H., Sy, S.M.H., Leung, J.W.C., Huen, M.S.Y., 2020. Screen identifies DYRK1B network as mediator of transcription repression on damaged chromatin. Proc. Natl. Acad. Sci. USA 117 (29), 17019–17030.
Eelen, G., de Zeeuw, P., Simons, M., Carmeliet, P., 2015. Endothelial cell metabolism in normal and diseased vasculature. Circ. Res 116 (7), 1231–1244.
Ewton, D.Z., Hu, J., Vilenchik, M., Deng, X., Luk, K.C., Polonskaia, A., Hoffman, A.F., Zipf, K., Boylan, J.F., Friedman, E.A., 2011. Inactivation of mirk/dyrk1b kinase targets quiescent pancreatic cancer cells. Mol. Cancer Ther. 10 (11), 2104–2114.
Fang, L.F., Zhong, G.P., Xie, Y.B., Liu, M.J., Ren, Y., Ye, X.L., Cen, D., 2018. Silencing of DYRK1B improves the sensitivity of human cervical carcinoma cells to cis-platinum. Int. J. Clin. Exp. Med. 11 (11), 11921–11930.
Fedorov, O., Huber, K., Eisenreich, A., Filippakopoulos, P., King, O., Bullock, A.N., Szklarczyk, D., Jensen, L.J., Fabbro, D., Trappe, J., Rauch, U., Bracher, F., Knapp, S., 2011. Specific CLK inhibitors from a novel chemotype for regulation of alternative splicing. Chem. Biol. 18 (1), 67–76.
Fenton, M., Barker, S., Kurz, D.J., Erusalimsky, J.D., 2001. Cellular senescence after single and repeated balloon catheter denudations of rabbit carotid arteries. Arterioscler. Thromb. Vasc. Biol. 21 (2), 220–226.
Gao, J., Zhao, Y., Lv, Y., Chen, Y., Wei, B., Tian, J., Yang, Z., Kong, F., Pang, J., Liu, J., Shi, H., 2013. Mirk/Dyrk1B mediates G0/G1 to S phase cell cycle progression and cell survival involving MAPK/ERK signaling in human cancer cells. Cancer Cell Int 13 (1), 2.
Gonzalez-Gualda, E., Baker, A.G., Fruk, L., Munoz-Espin, D., 2021. A guide to assessing cellular senescence in vitro and in vivo. FEBS J. 288 (1), 56–80.
Hadi, H.A., Suwaidi, J.A., 2007. Endothelial dysfunction in diabetes mellitus. Vasc. Health Risk Manag 3 (6), 853–876.
Haidari, M., Zhang, W., Willerson, J.T., Dixon, R.A., 2014. Disruption of endothelial adherens junctions by high glucose is mediated by protein kinase C-beta-dependent vascular endothelial cadherin tyrosine phosphorylation. Cardiovasc Diabetol. 13, 105.
Harris, E.S., Nelson, W.J., 2010. VE-cadherin: at the front, center, and sides of endothelial cell organization and function. Curr. Opin. Cell Biol. 22 (5), 651–658.
Hickson, L.J., Langhi Prata, L.G.P., Bobart, S.A., Evans, T.K., Giorgadze, N., Hashmi, S.K., Herrmann, S.M., Jensen, M.D., Jia, Q., Jordan, K.L., Kellogg, T.A., Khosla, S., Koerber, D.M., Lagnado, A.B., Lawson, D.K., LeBrasseur, N.K., Lerman, L.O., McDonald, K.M., McKenzie, T.J., Passos, J.F., Pignolo, R.J., Pirtskhalava, T., Saadiq, I.M., Schaefer, K.K., Textor, S.C., Victorelli, S.G., Volkman, T.L., Xue, A., Wentworth, M.A., Wissler Gerdes, E.O., Zhu, Y., Tchkonia, T., Kirkland, J.L., 2019. Senolytics decrease senescent cells in humans: Preliminary report from a clinical trial of Dasatinib plus Quercetin in individuals with diabetic kidney disease. EBioMedicine 47, 446–456.
Hu, J., Friedman, E., 2010. Depleting mirk kinase increases cisplatin toxicity in ovarian cancer cells. Genes Cancer 1 (8), 803–811.
Jong, H.L., Mustafa, M.R., Vanhoutte, P.M., AbuBakar, S., Wong, P.F., 2013. MicroRNA 299-3p modulates replicative senescence in endothelial cells. Physiol. Genom. 45 (7), 256–267.
Katsuumi, G., Shimizu, I., Yoshida, Y., Minamino, T., 2018. Vascular senescence in cardiovascular and metabolic diseases. Front Cardiovasc Med 5, 18.
Kettle, J.G., Ballard, P., Bardelle, C., Cockerill, M., Colclough, N., Critchlow, S.E., Debreczeni, J., Fairley, G., Fillery, S., Graham, M.A., Goodwin, L., Guichard, S., Hudson, K., Ward, R.A., Whittaker, D., 2015. Discovery and optimization of a novel series of Dyrk1B kinase inhibitors to explore a MEK resistance hypothesis. J. Med Chem. 58 (6), 2834–2844.
Khan, S.Y., Awad, E.M., Oszwald, A., Mayr, M., Yin, X., Waltenberger, B., Stuppner, H., Lipovac, M., Uhrin, P., Breuss, J.M., 2017. Premature senescence of endothelial cells upon chronic exposure to TNFalpha can be prevented by N-acetyl cysteine and plumericin. Sci. Rep. 7, 39501.
Kida, Y., Zullo, J.A., Goligorsky, M.S., 2016. Endothelial sirtuin 1 inactivation enhances capillary rarefaction and fibrosis following kidney injury through Notch activation. Biochem Biophys. Res Commun. 478 (3), 1074–1079.
Kimura, M., Dietrich, H.H., Huxley, V.H., Reichner, D.R., Dacey Jr., R.G., 1993. Measurement of hydraulic conductivity in isolated arterioles of rat brain cortex. Am. J. Physiol. 264 (6 Pt 2), H1788–H1797.
Kirkland, J.L., Tchkonia, T., 2020. Senolytic drugs: from discovery to translation. J. Intern Med 288 (5), 518–536.
Krouwer, V.J., Hekking, L.H., Langelaar-Makkinje, M., Regan-Klapisz, E., Post, J.A., 2012. Endothelial cell senescence is associated with disrupted cell-cell junctions and increased monolayer permeability. Vasc. Cell 4 (1), 12.
Kurz, D.J., Decary, S., Hong, Y., Erusalimsky, J.D., 2000. Senescence-associated (beta)-galactosidase reflects an increase in lysosomal mass during replicative ageing of human endothelial cells. J. Cell Sci. 113 (Pt 20), 3613–3622.
Lapytsko, A., Kollarovic, G., Ivanova, L., Studencka, M., Schaber, J., 2015. FoCo: a simple and robust quantification algorithm of nuclear foci. BMC Bioinforma. 16, 392.
Lee, K., Deng, X., Friedman, E., 2000. Mirk protein kinase is a mitogen-activated protein kinase substrate that mediates survival of colon cancer cells. Cancer Res 60 (13), 3631–3637.
Lee Walmsley, D., Murray, J.B., Dokurno, P., Massey, A.J., Benwell, K., Fiumana, A., Foloppe, N., Ray, S., Smith, J., Surgenor, A.E., Edmonds, T., Demarles, D., Burbridge, M., Cruzalegui, F., Kotschy, A., Hubbard, R.E., 2021. Fragment-Derived Selective Inhibitors of Dual-Specificity Kinases DYRK1A and DYRK1B. J. Med Chem. 64 (13), 8971–8991.
Lindberg, M.F., Meijer, L., 2021. Dual-Specificity, Tyrosine Phosphorylation-Regulated Kinases (DYRKs) and cdc2-Like Kinases (CLKs) in Human Disease, an Overview. Int J. Mol. Sci. 22 (11).
Lu, X., Huxley, V.H., Kassab, G.S., 2013. Endothelial barrier dysfunction in diabetic conduit arteries: a novel method to quantify filtration. Am. J. Physiol. Heart Circ. Physiol. 304 (3), H398–H405.
Mortuza, R., Chen, S., Feng, B., Sen, S., Chakrabarti, S., 2013. High glucose induced alteration of SIRTs in endothelial cells causes rapid aging in a p300 and FOXO regulated pathway. PLoS One 8 (1), e54514.
Muraki, M., Ohkawara, B., Hosoya, T., Onogi, H., Koizumi, J., Koizumi, T., Sumi, K., Yomoda, J., Murray, M.V., Kimura, H., Furuichi, K., Shibuya, H., Krainer, A.R., Suzuki, M., Hagiwara, M., 2004. Manipulation of alternative splicing by a newly developed inhibitor of Clks. J. Biol. Chem. 279 (23), 24246–24254.
Narasimhan, A., Flores, R.R., Robbins, P.D., Niedernhofer, L.J., 2021. Role of Cellular Senescence in Type II Diabetes. Endocrinology 162 (10).
Ock, S.A., Knott, J.G., Choi, I., 2020. Involvement of CDKN1A (p21) in cellular senescence in response to heat and irradiation stress during preimplantation development. Cell Stress Chaperon-.-. 25 (3), 503–508.
Orsenigo, F., Giampietro, C., Ferrari, A., Corada, M., Galaup, A., Sigismund, S., Ristagno, G., Maddaluno, L., Koh, G.Y., Franco, D., Kurtcuoglu, V., Poulikakos, D., Baluk, P., McDonald, D., Grazia Lampugnani, M., Dejana, E., 2012. Phosphorylation of VE-cadherin is modulated by haemodynamic forces and contributes to the regulation of vascular permeability in vivo. Nat. Commun. 3, 1208.
Oubaha, M., Miloudi, K., Dejda, A., Guber, V., Mawambo, G., Germain, M.A., Bourdel, G., Popovic, N., Rezende, F.A., Kaufman, R.J., Mallette, F.A., Sapieha, P., 2016. Senescence-associated secretory phenotype contributes to pathological angiogenesis in retinopathy. Sci. Transl. Med 8 (362), 362ra144.
Paliwal, S., de Giorgio, A., Neil, D., Michel, J.B., Lacoste, A.M., 2020. Preclinical validation of therapeutic targets predicted by tensor factorization on heterogeneous graphs. Sci. Rep. 10 (1), 18250.
Potter, M.D., Barbero, S., Cheresh, D.A., 2005. Tyrosine phosphorylation of VE-cadherin prevents binding of p120- and beta-catenin and maintains the cellular mesenchymal state. J. Biol. Chem. 280 (36), 31906–31912.
Prattichizzo, F., De Nigris, V., Mancuso, E., Spiga, R., Giuliani, A., Matacchione, G., Lazzarini, R., Marcheselli, F., Recchioni, R., Testa, R., La Sala, L., Rippo, M.R., Procopio, A.D., Olivieri, F., Ceriello, A., 2018. Short-term sustained hyperglycaemia fosters an archetypal senescence-associated secretory phenotype in endothelial cells and macrophages. Redox Biol. 15, 170–181.
Rhinn, M., Ritschka, B., Keyes, W.M., 2019. Cellular senescence in development, regeneration and disease. Development 146 (20).
Richardson, P., Griffin, I., Tucker, C., Smith, D., Oechsle, O., Phelan, A., Rawling, M., Savory, E., Stebbing, J., 2020. Baricitinib as potential treatment for 2019-nCoV acute respiratory disease. Lancet 395 (10223), e30–e31.
Sako, Y., Ninomiya, K., Okuno, Y., Toyomoto, M., Nishida, A., Koike, Y., Ohe, K., Kii, I., Yoshida, S., Hashimoto, N., Hosoya, T., Matsuo, M., Hagiwara, M., 2017. Development of an orally available inhibitor of CLK1 for skipping a mutated dystrophin exon in Duchenne muscular dystrophy. Sci. Rep. 7, 46126.
Salminen, A., Kauppinen, A., Kaarniranta, K., 2012. Emerging role of NF-kappaB signaling in the induction of senescence-associated secretory phenotype (SASP). Cell Signal 24 (4), 835–845.
Sharma, A., Tiwari, S., Deb, M.K., Marty, J.L., 2020. Severe acute respiratory syndrome coronavirus-2 (SARS-CoV-2): a global pandemic and treatment strategies. Int. J. Antimicrob. Agents 56 (2).

Soppa, U., Becker, W., 2015. DYRK protein kinases. Curr. Biol. 25 (12), R488–R489.
Sturmlechner, I., Durik, M., Sieben, C.J., Baker, D.J., van Deursen, J.M., 2017. Cellular senescence in renal ageing and disease. Nat. Rev. Nephrol. 13 (2), 77–89.
Sun, X., Kim, A., Nakatani, M., Shen, Y., Liu, L., 2016. Distinctive molecular responses to ultraviolet radiation between keratinocytes and melanocytes. Exp. Dermatol. 25 (9), 708–713.
Tanikawa, M., Sanjiv, K., Helleday, T., Herr, P., Mortusewicz, O., 2016. The spliceosome U2 snRNP factors promote genome stability through distinct mechanisms; transcription of repair factors and R-loop processing. Oncogenesis 5.
Triana-Martinez, F., Loza, M.I., Dominguez, E., 2020. Beyond Tumor Suppression: Senescence in Cancer Stemness and Tumor Dormancy. Cells 9 (2).
Tsuji, H., Otsuka, R., Wada, H., Murata, T., Sasaki, A., Itoh, M., Baghdadi, M., Sasaki, E., Seino, K.I., 2020. Induction of macrophage-like immunosuppressive cells from common marmoset ES cells by stepwise differentiation with DZNep. Sci. Rep. 10 (1), 12625.
Tzima, E., Irani-Tehrani, M., Kiosses, W.B., Dejana, E., Schultz, D.A., Engelhardt, B., Cao, G., DeLisser, H., Schwartz, M.A., 2005. A mechanosensory complex that mediates the endothelial cell response to fluid shear stress. Nature 437 (7057), 426–431.
Uzor, S., Porazinski, S.R., Li, L., Clark, B., Ajiro, M., Iida, K., Hagiwara, M., Alqasem, A. A., Perks, C.M., Wilson, I.D., Oltean, S., Ladomery, M.R., 2021. CDC2-like (CLK) protein kinase inhibition as a novel targeted therapeutic strategy in prostate cancer. Sci. Rep. 11 (1), 7963.
Vasko, R., Xavier, S., Chen, J., Lin, C.H., Ratliff, B., Rabadi, M., Maizel, J., Tanokuchi, R., Zhang, F., Cao, J., Goligorsky, M.S., 2014. Endothelial sirtuin 1 deficiency perpetrates nephrosclerosis through downregulation of matrix metalloproteinase-14: relevance to fibrosis of vascular senescence. J. Am. Soc. Nephrol. 25 (2), 276–291.
Verzola, D., Gandolfo, M.T., Gaetani, G., Ferraris, A., Mangerini, R., Ferrario, F., Villaggio, B., Gianiorio, F., Tosetti, F., Weiss, U., Traverso, P., Mji, M., Deferrari, G., Garibotto, G., 2008. Accelerated senescence in the kidneys of patients with type 2 diabetic nephropathy. Am. J. Physiol. Ren. Physiol. 295 (5), F1563–F1573.
Wagner, M., Hampel, B., Bernhard, D., Hala, M., Zwerschke, W., Jansen-Durr, P., 2001. Replicative senescence of human endothelial cells in vitro involves G1 arrest, polyploidization and senescence-associated apoptosis. Exp. Gerontol. 36 (8), 1327–1347.
Wang, L., Chung, J., Gill, S.E., Mehta, S., 2019. Quantification of adherens junction disruption and contiguous paracellular protein leak in human lung endothelial cells under septic conditions. Microcirculation 26 (3), e12528.
Wu, X., Moimas, S., Hopf, R., Giampietro, C., Kourouklis, A., Falk, V., Mazza, E., Ferrari, A., 2021. A free-form patterning method enabling endothelialization under dynamic flow. Biomaterials 273.
Xu, M., Pirtskhalava, T., Farr, J.N., Weigand, B.M., Palmer, A.K., Weivoda, M.M., Inman, C.L., Ogrodnik, M.B., Hachfeld, C.M., Fraser, D.G., Onken, J.L., Johnson, K. O., Verzosa, G.C., Langhi, L.G.P., Weigl, M., Giorgadze, N., LeBrasseur, N.K., Miller, J.D., Jurk, D., Singh, R.J., Allison, D.B., Ejima, K., Hubbard, G.B., Ikeno, Y., Cubro, H., Garovic, V.D., Hou, X., Weroha, S.J., Robbins, P.D., Niedernhofer, L.J., Khosla, S., Tchkonia, T., Kirkland, J.L., 2018. Senolytics improve physical function and increase lifespan in old age. Nat. Med 24 (8), 1246–1256.
Zhang, H., Holden-Wiltse, J., Wang, J., Liang, H., 2013. A strategy to model nonmonotonic dose-response curve and estimate IC50. PLoS One 8 (8), e69301.
Zhang, X., Wu, X., Tang, W., Luo, Y., 2012. Loss of p16(Ink4a) function rescues cellular senescence induced by telomere dysfunction. Int J. Mol. Sci. 13 (5), 5866–5877.
Zoico, E., Nori, N., Darra, E., Tebon, M., Rizzatti, V., Policastro, G., De Caro, A., Rossi, A. P., Fantin, F., Zamboni, M., 2021. Senolytic effects of quercetin in an in vitro model of pre-adipocytes and adipocytes induced senescence. Sci. Rep. 11 (1), 23237.